Supplementary material for Increase in precipitation scavenging contributes to long-term reductions of black carbon in the Arctic."
by Heslin-Rees et al.

Contents

1 Data availability

Figure S1 shows the available data used in this study, and periods in which the instruments overlap and intercomparisons between the measurements can be made.

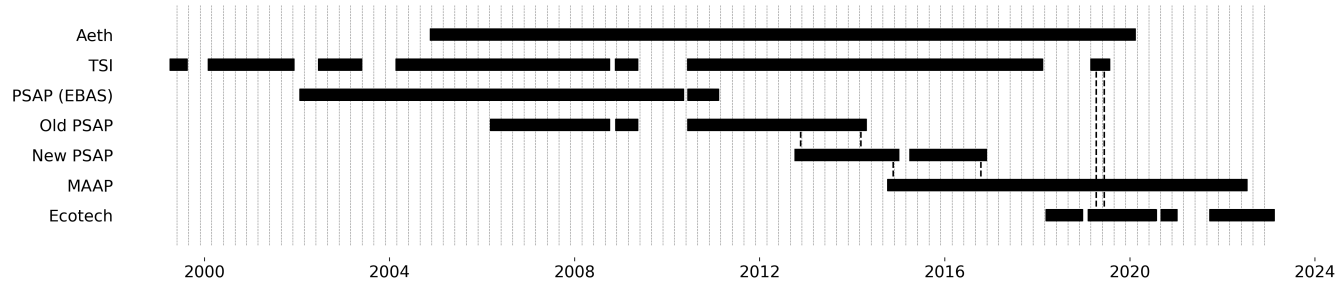

Figure S1. Data availability: the data deemed usable and valid are presented as a horizontal line plot. Missing data, when the instrument experienced problems or was away for servicing, are displayed as gaps in the line plot. All the instruments used in this study are presented and the periods in which intercomparisons were performed are signalled by the space between the dashed vertical lines. The MAAP and the automatic PSAP overlapped during the period between the 19^{th} of November 2014 to the 13^{th} of October 2016. The manual PSAP and the automatic PSAP overlapped between 19^{th} of November 2012 to 21^{st} March 2013

2 Harmonisation

2.1 Treatment of PSAPs

For the "automatic PSAP" and "manual PSAP", each filter was plotted separately, so that intensity (I) and volume (Q) could be visually inspected. In general, I, monotonically decreases over time as aerosol particles, in particular light-absorbing aerosols, settle on the filters. A threshold of 0.5 for the ratio between the measured transmittance and initial transmittance (τ) is set for when the exposed filter surface was changed; the build-up of aerosol particles can cause artefacts and hence the ratio cannot be too low. The σ_{ap} is then calculated based on the Bond correction scheme (see eq. 1), using a time step of 15 minutes for the "manual PSAP". The Bond correction scheme includes the influence of scattering particles via the SSA (single-scattering albedo). The light scattering coefficient (σ_{sp}) is provided by the Nephelometer. For periods in which nephelometer measurements were invalid or not present, Mie-derived scattering from the aerosol size distribution measured by a Differential Mobility Particle Sizer (DMPS) at Zeppelin station was used to estimate σ_{sp} (with an assumed refractive index of m = 1.544+0i). It is understood there are substantial uncertainties, however, for the purposes of simply correcting the PSAP measurements, the use of the DMPS-derived Mie scattering is considered acceptable (Zieger et al., 2010).

Bond et al. (1999) describes these corrections in detail. It should be added that no flow corrections, nor spot size corrections were applied to the data. The formula for the Bond correction is as follows:

$$\sigma_{\mathrm{ap}}(t) = \frac{A}{Q \cdot \Delta t} \ln\left(\frac{I(t-\Delta t)}{I(t)}\right) \cdot \frac{1}{1.37 \cdot \tau + 0.866} - 0.016 \cdot \sigma_{\mathrm{sp}}, \tag{1}$$

where σ_{ap} is the absorption coefficient, A is the Area of the sample spot/filter area [m^2], Q is the flow rate [given in litres per minute, but converted to m^3/minute], Δt is the time step used for integrating the measurements (e.g. 15 mins), I(t-Δ t) is the filter transmittance at time, t-Δ t, and I(t) is the filter transmittance at time, t. τ is the filter transmission (i.e. I/I_0) and σ_{sp} is the scattering coefficient.

It should be noted that the automatic PSAP initially showed instability, with strong fluctuations in I/I_0, however, a resolution of 1 hour applied to data processed with a running mean of 20 minutes resolves the issue. It is likely that the observed increase in noise is the result of large fluctuations in the sample flow due to an improper trigger algorithm to set the sample flow.

Prior to 2006-04-20, σ_{ap} is acquired from EBAS (http://ebas.nilu.no/, last access: 07 01 2022).

2.2 Treatment of MAAP data

The MAAP operates at a constant flow rate of $1000\,\mathrm{l\,hr^{-1}}$, and data was deemed invalid if the flow rate decreased below $900\,\mathrm{l\,hr^{-1}}$. It is assumed that the NOAA software does most of the interpretation internally and just outputs a missing value code if the data is affected. The NOAA software additionally converts the parameters to STP (as signified by the 0x0200 system flag). All erroneous data were removed before taking hourly arithmetic means. The MAAP operated at a resolution of around 1-2 minutes.

Only values greater than $0\,\mathrm{Mm^{-1}}$ were considered valid. This is despite the stated detection limit by the manufacturers, for a 30-minute time resolution, being approximately $<0.13\,\mathrm{Mm^{-1}}$ (or $20\,\mathrm{ng\,m^{-3}}$).

2.3 Harmonisation

The time series for the σ_{ap} measurements is composed of different instruments which have each respectively undergone several changes e.g. maintenance and calibration. Therefore, it is important to show the temporal evolution of these changes in relation to the other instruments (see Fig S2 and S4). The comparison between the MAAP and automatic PSAP shows a fairly stable relation, with a semi-constant correction factor. Despite, a 3-month period where the automatic PSAP exhibited values 4 times greater than the manual PSAP, an average of 2.11 is considered to represent the relation between the two instruments.

The correction factors are applied to various time periods to produce the harmonised full-time series displayed in Figure S3. Measurements from the automatic PSAP were multiplied by the correction factor (CF) of 0.61. After this, the measurements from the automatic PSAP with the CF applied were compared to the manual PSAP; a value of 1.30 was applied to the manual PSAP. Finally, a CF of 1.20 was applied to the data set from EBAS. Despite, the EBAS data set and the data processed from the manual PSAP. The reason for the scatter can be small differences in any of the variables that enter the calculations.

The equation for converting σ_{ap} from one wavelength to another is given as follows:

$$\sigma_{\mathrm{ap}}^{\lambda_2} = \sigma_{\mathrm{ap}}^{\lambda_1} \left(\frac{\lambda_1}{\lambda_2} \right)^{\mathrm{AAE}}, \tag{2}$$

where λ_1 and λ_2 are the wavelengths, and AAE is the Absorbing Ångström Exponent. This utilises the $1/\lambda$ dependence and is based on the "small particle limit" theory (Hulst and van de Hulst, 1981) and hence to adjust for example from 525 nm to 637 nm, $\sigma_{\mathrm{ap}}^{637} = \sigma_{\mathrm{ap}}^{525}(525/627)$ is used.

σ_{ap} measured and recorded by the PSAPs was converted from 525 nm (wavelength the PSAP operates on) to 637 nm. The conversion was done by assuming an Absorbing Ångström Exponent (ÅAE) of 1 (i.e. pure EC) (see Eq.2). Examining the ÅAE from the Aethalometer data this was considered a fair assumption.

The Theil-Sen slope estimator (TS) was used to calculate the gradient of the slope for each intercomparison; for robustness, a simple least-mean-squares approach (LMS) was also utilised, however, the CF was determined based on the TS result. For the intercomparisons only values between 0 - $3.5\,\mathrm{Mm^{-1}}$ were used, so that extreme values did not affect the intercomparisons too much. The correction factors are applied to the data as follows:

$$\sigma_{\mathrm{ap,CF}}^{637} = \frac{\sigma_{\mathrm{ap,uncor.}}^{637}}{\mathrm{CF}}, \tag{3}$$

where CF is the correction factor and $\sigma_{\mathrm{ap,uncor.}}^{637}$ simply represents the uncorrected data.

It should be noted that the most significant source of uncertainty for the PSAP measurements arises from the choice of a correction scheme e.g. Bond et al. (1999); Virkkula (2010); Ogren (2010). In this study, the PSAP measurements are compared with the MAAP measurements, and hence any uncertainties related to the choice of the correction scheme are embedded in the CF applied to the data.

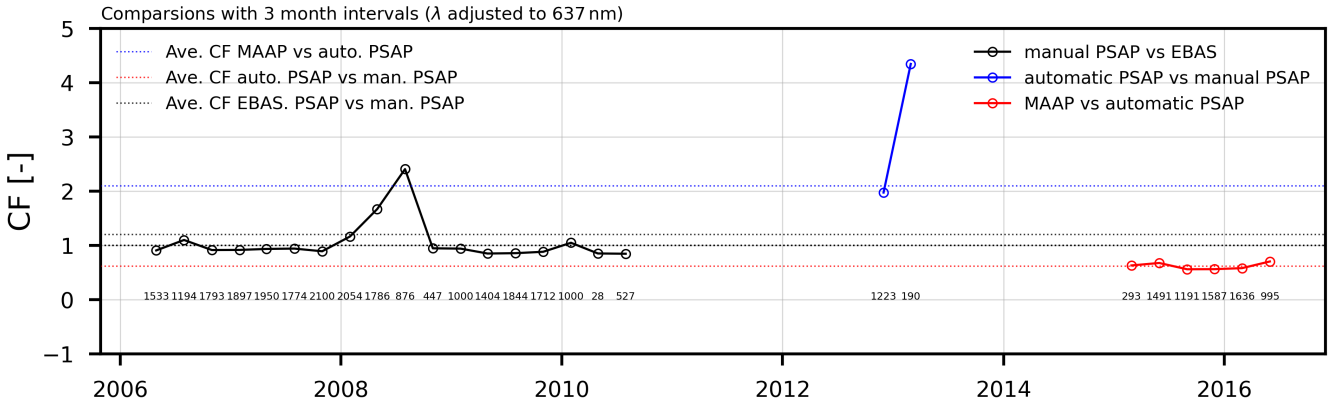

Figure S2. Harmonisation timeline: data from the different instruments are compared with one another to ascertain the coefficient of regression (using the Theil Sen Slope). The reciprocal is the correction factor (CF). Comparisons are done for every 3-month intervals. The number of data points for each comparison is represented in the integer value below the line plots.

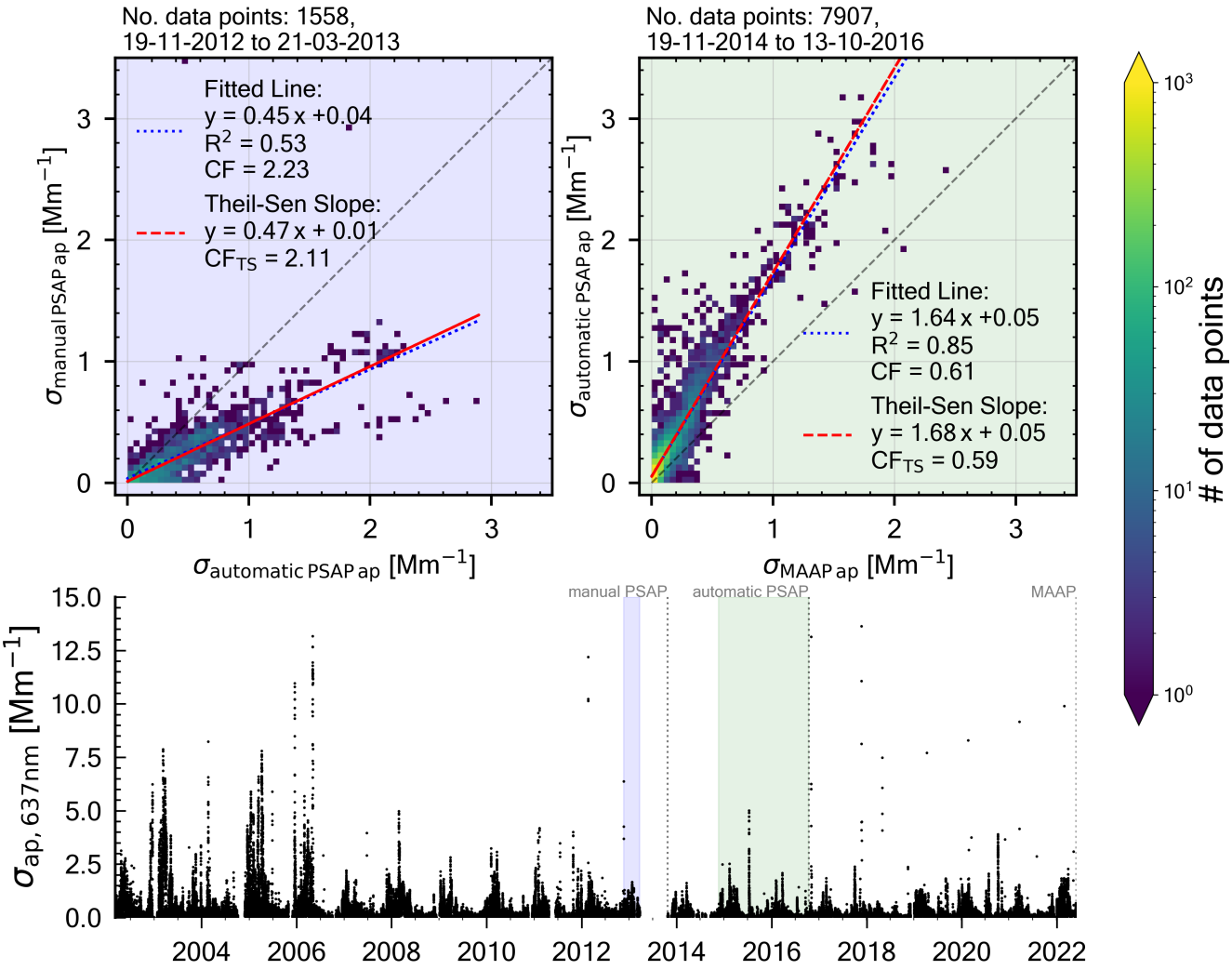

Figure S3. Harmonisation of the long-term absorption coefficient (σ_{ap}) data set: density plot shaded in blue (a) displaying the intercomparisons performed between the manual PSAP and automatic PSAP. The results of both the Theil-Sen slope estimator (TS) and least-mean-squares (LMS) approach are displayed in the top left, density plot shaded in green (b) displaying the intercomparison between the automatic PSAP and the MAAP. Both TS and LMS are displayed in the top left, and time series of homogenised σ_{ap} measured at 637 nm (c). The shaded regions denote the respective period in which the instruments were measuring at the same time. The dashed vertical line denotes the end time of each respective instrument. Note that the correction factor (CF) for the manual PSAP vs. automatic PSAP is not the CF that is applied to the data.

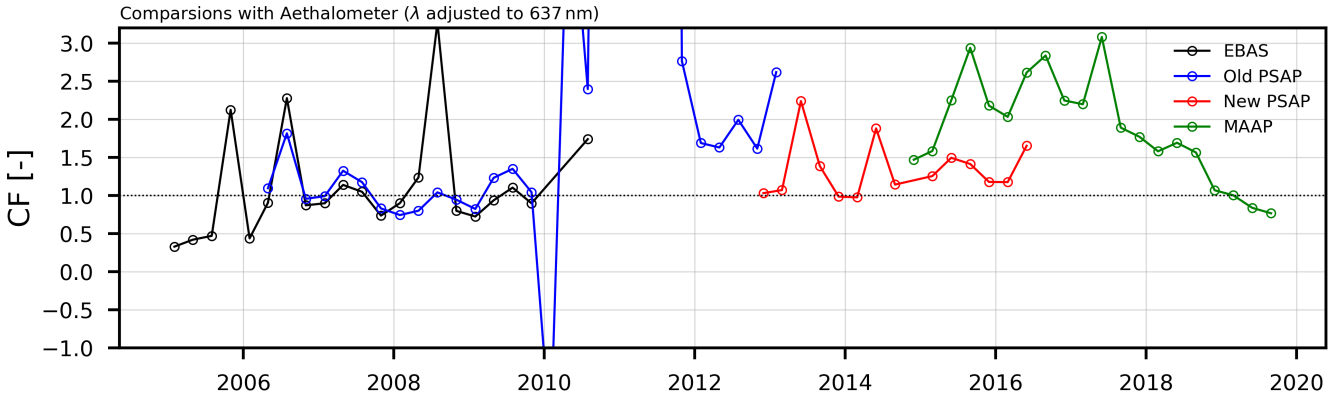

Figure S4. Harmonisation timeline with Aethalometer (A31): data from the different instruments are compared with one another to ascertain the coefficient of regression (using the Theil Sen Slope). The reciprocal is the correction factor (CF). Comparisons are done every 3-month intervals. Only comparisons where there were at least 50 data points are shown.

2.4 Nephelometer comparison: TSI vs. ecotech

For harmonisation, the TSI was used as the reference instrument (need to: reference as to why the TSI is better). Using an instrument-specific correction factor, the σ_{sp} values of the Ecotech were adjusted to match the TSI. Generally, the agreement between the two nephelometers was good (R^2 of ± 0.89), despite the overlap of available data being only 2 months. Furthermore, there were additional problems with the TSI from 2016 onwards. The problems with the TSI were likely caused by the instrument being stuck in the zeroing mode. Data from this period was used by taking only the measurements where the instrument was considered not to be in the zeroing operation mode. This procedure was able to be performed and the data were cleaned as these normal modes had a recurring pattern.

For the comparison, TSI σ_{sp} measurements at wavelengths 550 and 700 were adjusted to 525 and 635 nm and the wavelengths 525 and 635 of Ecotech σ_{sp} values were adjusted to 550 and 700 nm, using equation 4 and 2. Equation 2, is used to adjust σ_{sp} to any other wavelength λ_{x}, see Müller et al. (2011) for further details. For wavelength adjustment, the scattering Ångström exponent (SAE) is computed from the blue (450 nm) and green (550 nm) wavelengths.

$$\mathrm{SAE} = -\frac{\log\left(\sigma_{\mathrm{sp}}^{\lambda_1}/\sigma_{\mathrm{sp}}^{\lambda_2}\right)}{\log\left(\lambda_1/\lambda_2\right)} \tag{4}$$

For the adjustment of the scattering coefficient, AAE in equation 2 is substituted as the Scattering Ångström Exponent (SAE).

The Ecotech typically overestimates the scattering coefficients when compared to the TSI. SSA is given in terms of wavelength 637 nm, hence the TSI and Ecotech σ_{sp} are adjusted.

3 Assigning clusters:

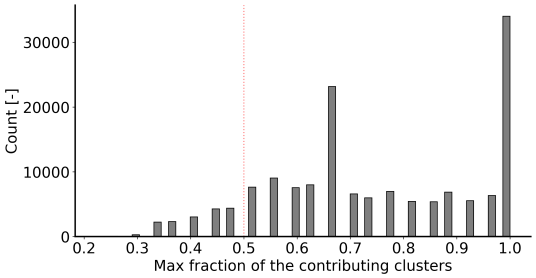

Figure S5. Frequency plot for the maximum proportion of one particular cluster for a given observation. For an ensemble of 27 back trajectories the majority of observations were tied to one or more back trajectory clusters, hence values below 1. If the observation had almost equal contribution from all clusters (i.e. $\sim$ 5/27 would be the maximum fraction for this)

4 MODIS calculations

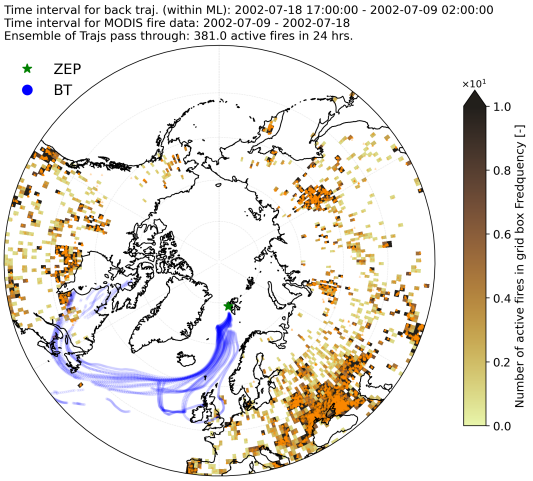

Figure S6. Example plot: a back trajectory arriving at Zeppelin Observatory 01:00:00 on the 19th of July 2002 is displayed. The back trajectory is marked in red. The active forest fires are displayed as orange triangles. The number of active fires at any given time has been calculated and coloured according to the number of fires present in that grid; this is displayed by the colour bar. All active fire data is derived by the MODIS Satellite. For this given timestamp, grids were traversed containing a total of 384 active fires.

5 Trend analysis of the last 7 years:

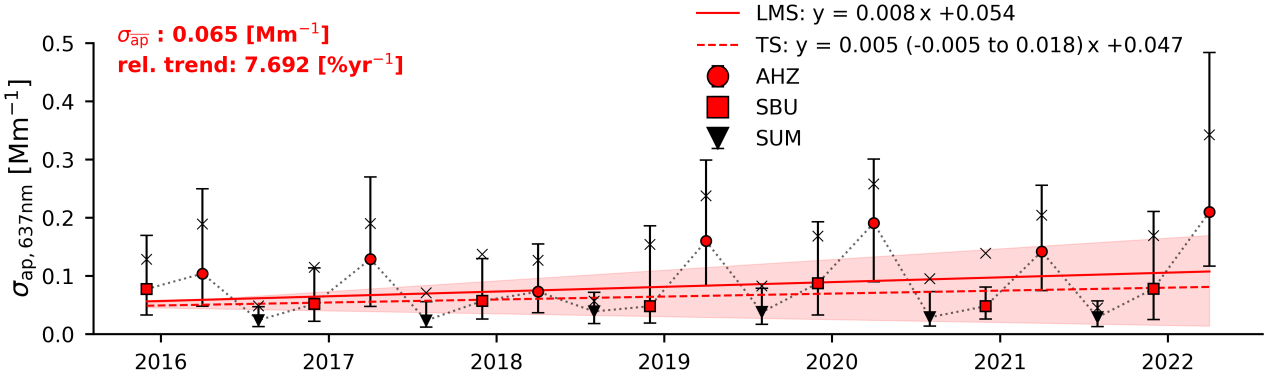

Figure S7. MAAP time series for the absorption coefficient (σ_{ap}) measured at Zeppelin observatory for the last 6 full years of data (2015-2022): seasonal medians are displayed as shapes, the Arctic Haze (AHZ) denoted by a red circle, the slow-build up (SBU) by a red square and summer (SUM) by a black triangle. The Theil-Sen Slope (TS) trend line is displayed as a dashed red line with a red-shaded region corresponding to 95% significance. The least-mean square (LMS) is presented as a solid red line. The trend lines are both calculated using the seasonal medians, as opposed to seasonal means (X). The overall median for the data set is displayed in the top left. it should be noted that at least 5 year's worth of long-term data is required to perform any reliable trend analysis.

6 Long-term trends in Single Scattering Albedo (SSA)

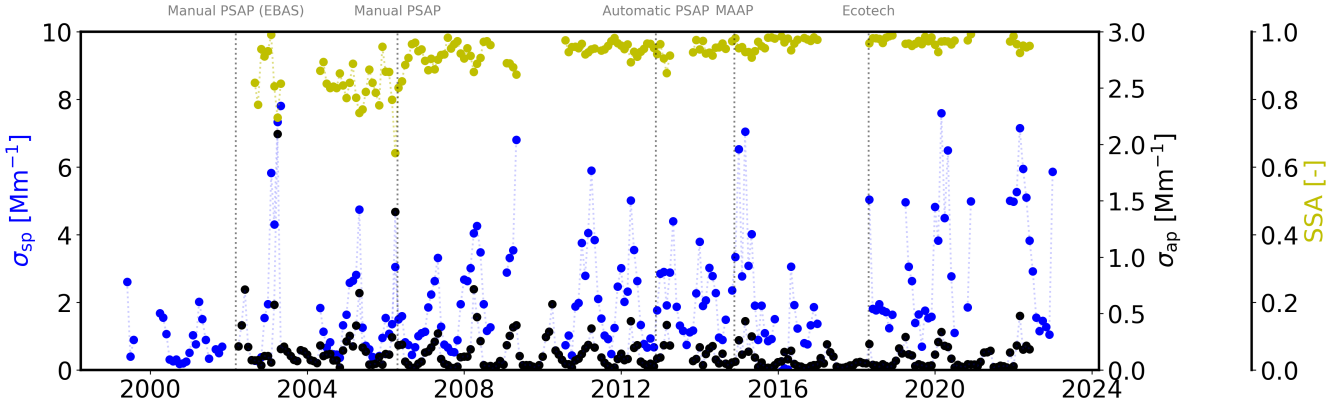

Figure S8. Comparing harmonised absorption coefficient with the single scattering albedo (SSA) and scattering coefficient:

7 Concentration weighted trajectory mappings

Figure S9, displays the spatial variation in the CWT σ_{ap} value. The largest contributions come from Eurasia. It is also worth noting the various forest fire events, in particular the fire in May 2006 in Eastern Europe that was effectively transported to the Arctic (Stohl et al., 2007), and the fire during the 10-17 th of July 2015 in the Yukon-Koyukuk state of Alaska.

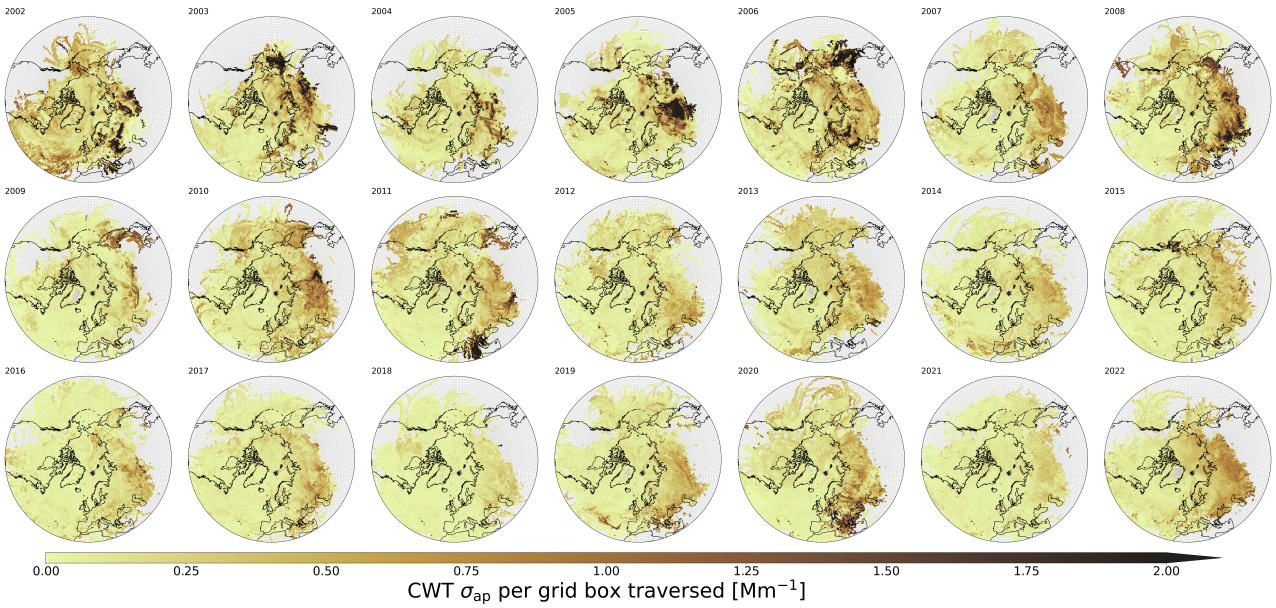

Figure S9. CWT values for σ_{ap} for each year of data from 2002 to 2022.

8 Trends in ECLIPSE V6b global emission fields:

The figure,S10 uses the emission inventories from the ECLIPSE V6b global emission fields for 2000, 2005, 2010, 2015 and 2020 to calculate the trend for each grid cell. The majority of regions display decreasing trends for those emission inventory data sets. However, parts of the middle east, central Asia and north Africa exhibit increasing trends.

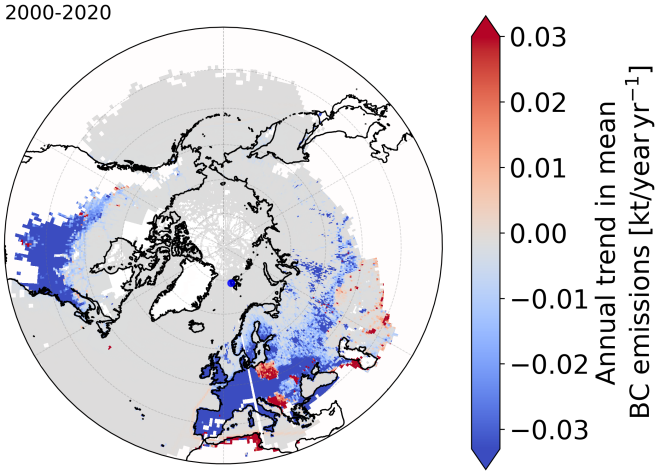

Figure S10. Spatial trend for the BC emissions per a grid cell for the ECLIPSE V6b global emission fields for 2000, 2005, 2010, 2015 and 2020. The map is masked based on the spatial coverage of the HYSPLIT endpoints.

9 Annual frequency of five clusters:

The annual cycle for the five clusters is composed of the data between 2002 and 2022.

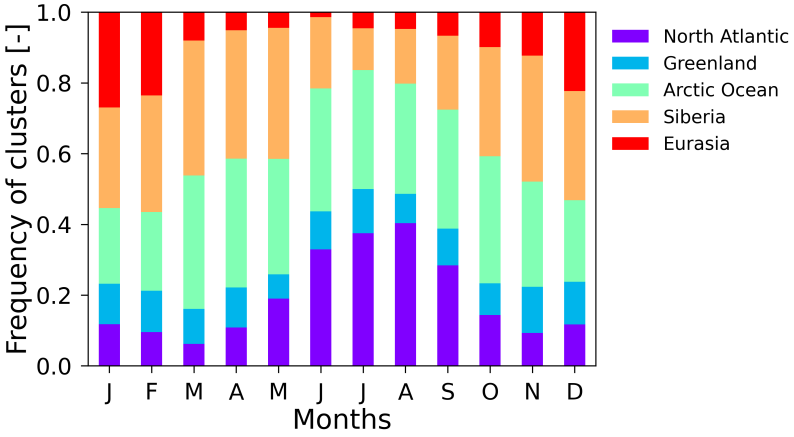

Figure S11. The proportion of the various clusters for each month.

10 Cluster trends:

The Eurasian cluster (i.e. red, cluster) is the only cluster that displays a positive long-term trend as described by the TS slope estimator (see Fig. S12).

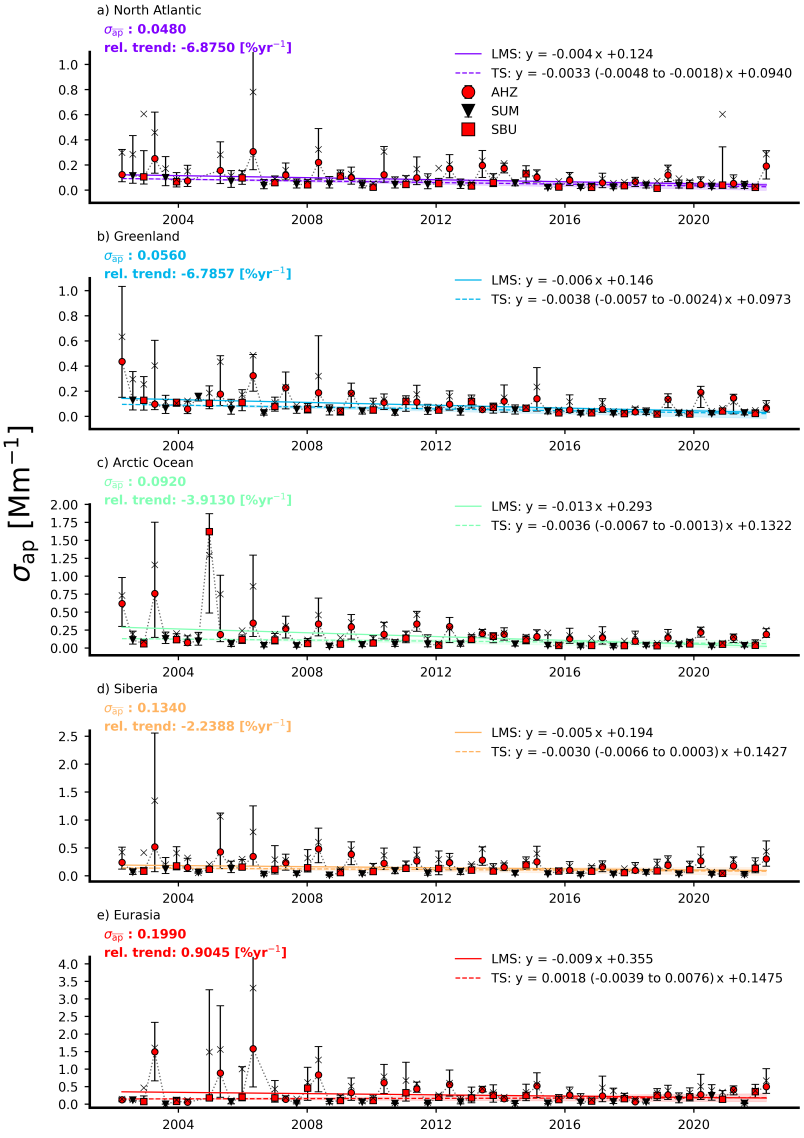

Figure S12. The time series for σ_{ap}, in terms of each cluster. Cluster analysis was performed using the latitude, longitude and altitude of all data points in the collocated data set. The length of each back trajectory was set at 10 days.

11 Seasonality:

From figure S13 c, the emission inventories collocated with the HYSPLIT back trajectories display a peak in the traditional winter (DJF), the Arctic Haze, however, as seen in figure S13 a, is slightly after the peaked observed in S13 c; this delay is argued to be the result in the slight dip in the sink effect brought about by a decline in ATP in MAM (see Fig. S13 b).

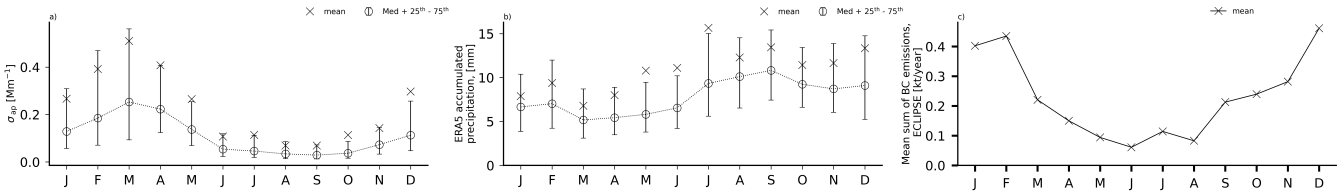

Figure S13. Seasonality plots for (a) the absorption coefficient, (b) the accumulated back trajectory precipitation (ATP) and (c) the emission inventory collected with the endpoint of the back trajectories.

12 Extreme wet days:

Extreme values are defined using the 99$^{\text{th}}$ percentile of the entire 21 years of data, 2002 - 2022. Values above the defined 99$^{\text{th}}$ percentile annual composition. We observe that 14 % of the "clean" days at ZEP, coincident with back trajectories which have experienced extremely high amounts of accumulated precipitation (i.e. "wet" conditions). We also observe that the proportion of clean days that coincident with extremely high ATP back trajectories has increased in the past 20 years, going from compromising of 7% of events to approximately 17%. In total 6 % of the arriving back trajectories were reported as having extremely high ATP values.

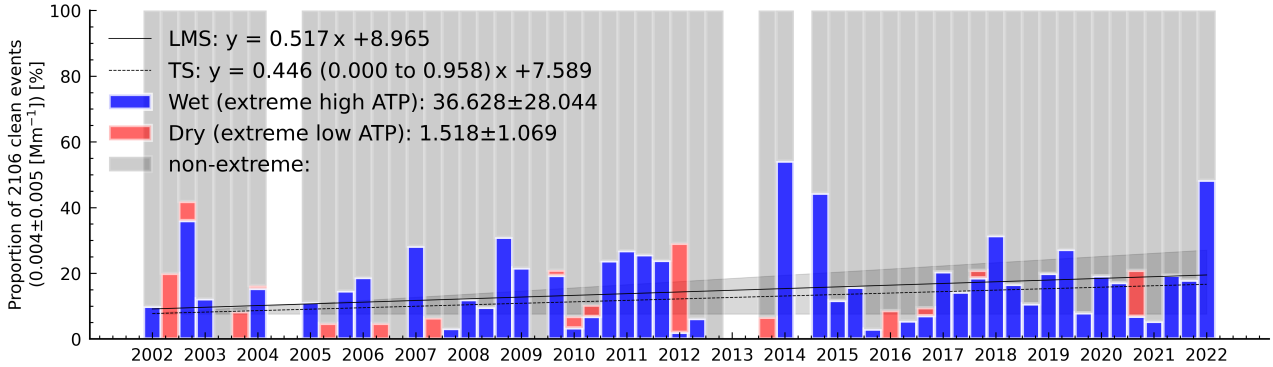

Figure S14.

13 Scavenging ratio:

The work presented here is in keeping with the work done by Garrett et al. (2010), for the carbon monoxide measurements (CO) the seasonal background value is estimated using the 5^{th} percentile. ΔCO is the difference between each subsequent 6 hour CO measurement. $\Delta CO > 3.2$ ppbv is selected such that the signal-to-noise ratio is sufficiently high (Garrett et al., 2010). The CO was downloaded from EBAS (http://ebas.nilu.no/). The normalisation, by ΔCO, of the aerosol parameter, is important to be able to assess the transport efficiency of anthropogenic pollution.

The proxy for the scavenging (see eq. 5) is calculated as follows:

$$S_{ap} = \frac{\Delta\sigma_{ap}}{\Delta\mathrm{CO}} = f_{ap}\frac{\Delta\sigma_{ap}}{\Delta\mathrm{CO}}, \tag{5}$$

where S_{ap} is the scavenging proxy, $\Delta\sigma_{ap}$ is the short-term perturbations in σ_{ap} (i.e. aerosol particles), and $\Delta\mathrm{CO}$ is the perturbations in CO.

When the S_{ap} is low, the aerosol removal is deemed to be high (i.e. a combination of both dry deposition and wet scavenging). The short-term perturbations in aerosols display a much stronger seasonal cycle than those for CO, and as such, it was suggested by Garrett et al. (2011) that the removal processes play a much stronger role in controlling the aerosol concentrations than the transport efficiency.

Moreover, Garrett et al. (2011) concluded, based on data from Barrow and Alert, that σ_{ap} and σ_{sp} are scavenged equally efficiently, suggesting that (hydrophobic BC) is being removed as readily as soluble inorganic salts. It is likely that this is because mid-latitude BC and soluble aerosols are internally mixed during transportation to the Arctic, and thus the scattering and absorbing components are removed together. It would be expected that larger aerosol particles (potentially more scattering particles e.g. sea salt aerosol) would be scavenged more easily. Coarse mode particles such as sea salt would be an example of an aerosol that would be removed more efficiently, as opposed to smaller aerosol types (Dadashazar et al., 2021; Galloway et al., 1993).

It is assumed that CO is much less sensitive to wet removal processes. However, CO levels were shown to vary depending on the amount of accumulated precipitation. Also, concentrations of aerosol particles can be influenced by sources closer to ZEP that can mask the aerosol response to wet scavenging during long-range transport.

In figure S15 the same analysis is applied on the scattering and absorption coefficient.

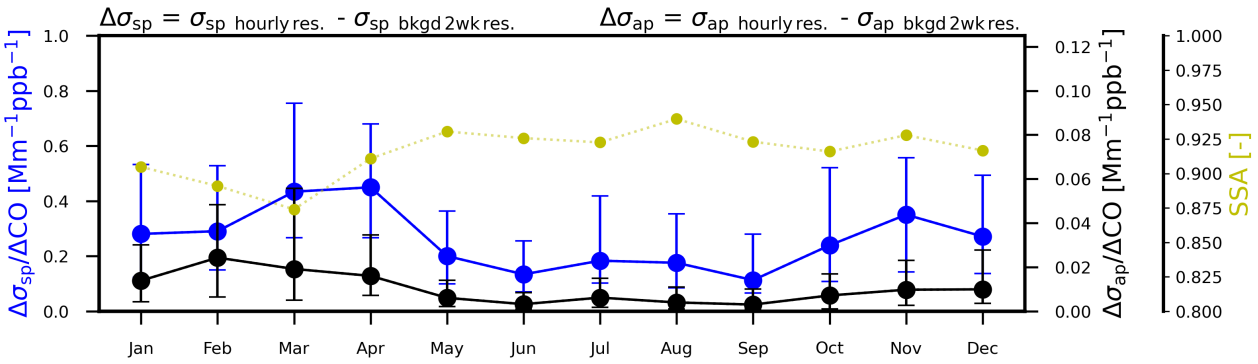

Figure S15. Sink proxy: monthly medians of the scavenging ratio S for light-absorbing aerosols, along with the 25^{th} and 75^{th} percentiles which are displayed as error bars. The scavenging ratio is calculated for hourly short-term perturbations in CO and σ_{ap}. When the scavenging ratio is low, aerosol removal has been high.

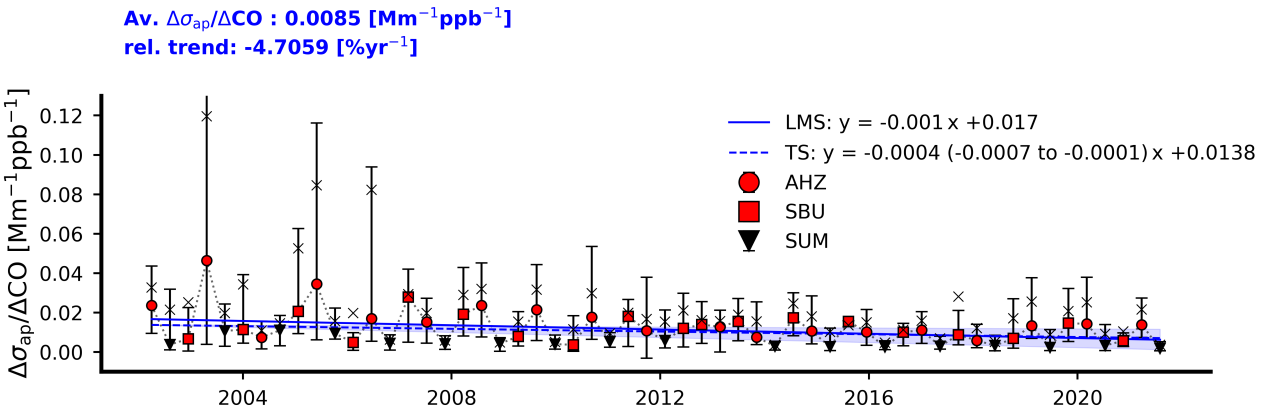

Figure S16. Long-term trend in the scavenging ratio, or sink proxy, for the absorption coefficient σ_{ap} (S_{ap}). S_{ap} represents the short-term perturbations in σ_{ap} relative to short-term perturbations in carbon monoxide (CO) measured at Zeppelin observatory. Seasonal means are displayed as shapes, the Arctic Haze (AHZ) denoted by a red circle, the slow-build up (SBU) by a red square and summer (SUM) by a black triangle. The Theil-Sen Slope (TS) trend line is displayed as a dashed blue line with a blue-shaded region corresponding to 95% significance. The least-mean square (LMS) is presented as a solid blue line. The trend lines are both calculated using seasonal means. The overall average for the data set in question is displayed in the top left.

14 Empirical relationships for the simulation/model:

For each cluster and season, the relationship between σ_{ap} and ATP is examined. Note that on this scale wet scavenging seems more efficient during AHZ, this is despite liquid precipitation being more effective than solid precipitation. Pollutants during SUM air masses appear scavenging before the 10-day back trajectories begin, suggesting that these summer air masses are already cleaned before they are transported up to the Arctic.

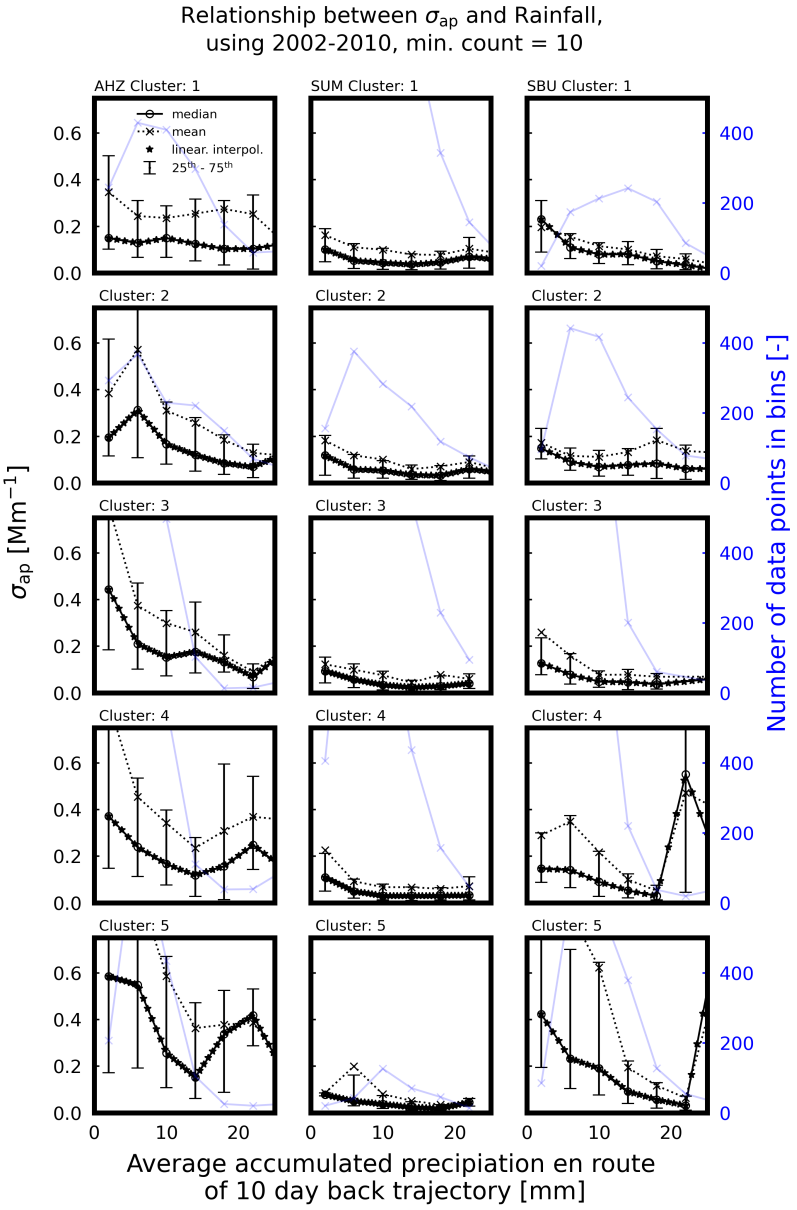

Figure S17. Empirical relationships for the simulation/model: the data is binned using a 2 mm interval. The median for each bin is then linearly interpolated to achieve a better resolution.

References

Bond, T. C., Anderson, T. L., and Campbell, D.: Calibration and intercomparison of filter-based measurements of visible light absorption by aerosols, Aerosol Science & Technology, 30, 582–600, 1999.

Dadashazar, H., Alipanah, M., Hilario, M. R. A., Crosbie, E., Kirschler, S., Liu, H., Moore, R. H., Peters, A. J., Scarino, A. J., Shook, M., et al.: Aerosol responses to precipitation along North American air trajectories arriving at Bermuda, Atmospheric chemistry and physics, 21, 16 121–16 141, 2021.

Galloway, J., Savoie, D., Keene, W., and Prospero, J.: The temporal and spatial variability of scavenging ratios for NSS sulfate, nitrate, methanesulfonate and sodium in the Atmosphere over the North Atalantic Ocean, Atmospheric Environment. Part A. General Topics, 27, 235–250, 1993.

Garrett, T., Zhao, C., and Novelli, P.: Assessing the relative contributions of transport efficiency and scavenging to seasonal variability in Arctic aerosol, Tellus B: Chemical and Physical Meteorology, 62, 190–196, 2010.

Garrett, T. J., Brattström, S., Sharma, S., Worthy, D. E., and Novelli, P.: The role of scavenging in the seasonal transport of black carbon and sulfate to the Arctic, Geophysical Research Letters, 38, 2011.

Hulst, H. C. and van de Hulst, H. C.: Light scattering by small particles, Courier Corporation, 1981.

Müller, T., Laborde, M., Kassell, G., and Wiedensohler, A.: Design and performance of a three-wavelength LED-based total scatter and backscatter integrating nephelometer, Atmospheric Measurement Techniques, 4, 1291–1303, 2011.

Ogren, J. A.: Comment on "Calibration and intercomparison of filter-based measurements of visible light absorption by aerosols", Aerosol Science and Technology, 44, 589–591, 2010.

Stohl, A., Berg, T., Burkhart, J., FjÆaa, A., Forster, C., Herber, A., Hov, Ø., Lunder, C., McMillan, W., Oltmans, S., et al.: Arctic smoke–record high air pollution levels in the European Arctic due to agricultural fires in Eastern Europe in spring 2006, Atmospheric Chemistry and Physics, 7, 511–534, 2007.

Virkkula, A.: Correction of the calibration of the 3-wavelength Particle Soot Absorption Photometer (3λ PSAP), Aerosol Science and Technology, 44, 706–712, 2010.

Zieger, P., Fierz-Schmidhauser, R., Gysel, M., Ström, J., Henne, S., Yttri, K. E., Baltensperger, U., and Weingartner, E.: Effects of relative humidity on aerosol light scattering in the Arctic, Atmospheric Chemistry and Physics, 10, 3875–3890, 2010.